

Hollow ion formation and decay in slow Bi^{46+} - C_{60} collisions

Uwe Thumm

J. R. Macdonald Laboratory, Department of Physics, Kansas State University, Manhattan, Kansas 66506

(Received 3 July 1996)

The interaction of slow highly charged ions with many-electron targets leads to the formation of unstable, multiply excited projectiles. We simulated the formation of such hollow ions for slow incident Bi^{46+} projectiles and C_{60} targets. Our semiclassical overbarrier simulation includes resonant exchange and Auger emission of electrons. It models the dynamical variation of level occupations and charge states during the collision and predicts highly unstable hollow ions immediately after the collision. With respect to the subsequent downstream relaxation of the hollow ions, we propose a simple relaxation scheme that includes autoionizing and radiative transitions. As a consequence of this downstream relaxation, almost all of the resonantly captured electrons are emitted. [S1050-2947(97)09201-9]

PACS number(s): 34.50.Bw, 34.70.+e, 82.30.Fi, 61.46.+w

I. INTRODUCTION

Within the past few years, the interaction of highly charged ions with metal [1–13] and insulating [14–18] surfaces and clusters [19–25] has been a subject of rapidly increasing experimental and theoretical interest. For grazing-incidence collisions with surfaces, recent experiments have measured the final charge-state distribution of the surface-scattered projectile [13], the deflection angle [26,18], and the emission of electrons [6,7,11,15] and photons [1,5,12] during and after the projectile surface interaction. More recently, insulating surfaces have been added to the list of target materials, and interesting phenomena have been seen, and traced to distinctly different electronic properties of insulator as compared with metal surfaces [15,17]. The most obvious differences between insulating and conducting targets are related to different conductivities that lead to the local accumulation of charges on insulators. These localized charges, in turn, influence the subsequent charge-transfer dynamics and the projectile trajectory. In general, an approaching projectile first captures electrons from the highest occupied target levels, i.e., from levels that are energetically close to the Fermi level. This means that the location of the Fermi level, i.e., the work function, becomes an important substrate-dependent parameter in the description of the charge-exchange process. The charge-transfer dynamics on insulating and metal surfaces also differs with respect to the availability of unoccupied surface states above the Fermi level of a metal, allowing for the recapture of an electron after a previously captured electron is energetically shifted across the Fermi level and into resonance with the unoccupied part of the conduction band. For insulators this resonant loss channel is closed, since a broadband gap is located above the Fermi level.

Cluster targets, in particular fullerenes, combine several of the above-mentioned features of charge transfer on metals and insulators. For clusters, electron capture leads to a charged target, as in the case of an insulating surface. Large metallic clusters have a band structure similar to metal surfaces with regard to a large portion of unoccupied states above the Fermi level. Smaller clusters tend to form narrow spaced levels, rather than bands, and, with regard to

capture, may resemble a large atomic target. In this work, we consider neutral C_{60} targets. By measuring both target and projectile charge states in coincidence, it has recently [19] become possible to separate soft and hard collisions. Soft collisions occur at relatively large impact parameters, result in the capture of a relatively small number of electrons, and do not lead to fragmentation of the target. For collisions of highly charged ions with surfaces, the image charge acceleration [26] imposes an upper limit for the closest approach of the projectile to the target, and complicates the distinction between above-, near-, and below-surface interactions [5,7,9]. In contrast, soft collisions with fullerenes (that to some extent may be viewed as spherically shaped monolayers of graphite surfaces) at large impact parameters allow for the undistorted investigation of above-surface effects. The electronic structure of neutral C_{60} is well understood from first-principles calculations [23,27–32]. In applications to charge exchange and electron emission in soft ion- C_{60} collisions, we have previously used two different models to represent the target electronic structure. We first [21,22] used the local-density approximation (LDA) description of Puska and Nieminen [33], which models the behavior of the 240 valence electrons based on a smeared out, attractive background potential of all 60 carbon cores. Next [23], we employed a more accurate molecular self-consistent Dirac-Fock-Slater (DFS) calculation [27] to obtain ground-state electronic structures of neutral C_{60} and its positive ions C_{60}^{i+} , $i=0 \dots 6$. In comparison with the LDA calculation of Puska and Nieminen [33], the DFS calculation shows noticeable differences in the calculated valence spectra of neutral C_{60} . However, the comparison of scattering calculations based on the two different descriptions of the target-electronic structure [23] shows that cross sections for the production of specific target-charge states in soft collisions, charge-state evolutions of target and projectile, and projectile scattering angles agree at the 10% level. With respect to cross sections for charge-state-changing 80-keV Ar^{8+} - C_{60} collisions, our scattering simulations based on the LDA and DFS target electronic structure calculations agree within the overall accuracy of our model, and are in fair agreement with experiments [19].

A number of attempts to model the relaxation of multiply

excited ions have been made in the past. Benoit-Cattin *et al.* [34] investigated the relaxation of doubly, triply, and quadruply excited projectile states formed in collisions of 70-keV N^{7+} ions with Ar. Their discussion of possible relaxation paths is based on measured electron spectra in conjunction with predictions of the classical overbarrier model of Niehaus [35] for the formation of the hollow ion. The emitted electron spectra are dominated by doubly excited lines which are traced to excited states formed by either direct double capture or autoionizing cascades. As the authors admit, the assessment of particular decay paths is very difficult, even for the case of a bare incident ion presumably leading to, at the very most, quadruply excited states. Radiative stabilization following double-electron capture of 10 keV/amu Ar^{q+} , $q \leq 17$, and Kr^{q+} , $q \leq 34$, ions colliding with Ar was discussed by Ali *et al.* [36]. Radiative stabilization was found to be of importance for the case of asymmetric doubly excited states, where the two excited electrons populate shells of different principal quantum numbers, $n \ll n'$. These states may be the result of double capture into shells of comparable principal quantum numbers ($n \approx n'$) followed by an Auger transition, as suggested by Roncin, Gaboriaud, and Barat [37]. The radiative relaxation cascade is then assumed to proceed along the ‘‘Yrast’’ line of maximal angular momentum of the active electron. This is supported by the statistical dominance of high angular momentum states, the dipole selection rule ($\Delta l = 1$), and the resonant population of high angular momentum states at large impact parameters. For multiply charged argon ions (Ar^{q+} , $q = 5 \cdots 17$) colliding with neutral argon at 10 keV/amu, a relaxation scheme based on Auger transitions has been suggested by Ali *et al.* [38]. Many assumptions in this scheme are similar to the discussions of Benoit–Cattin *et al.* [34] and Posthumus and Morgenstern [39]. However, the relaxation was assumed to proceed along one particular decay path determined as the sequence of most likely relaxation steps, whereas different paths were taken into consideration in Refs. [34] and [39].

On the theoretical side, Vaeck and Hansen [40,41], van der Hart and Hansen [42], and Hansen, Schraa, and Vaeck [43] recently calculated radiative and Auger decay rates for multiply excited ions. These *ab initio* calculations predict that, for increasing asymmetry of a doubly excited state, autoionization becomes less important, and radiative transitions possible. Close-coupling calculations by Chen and Lin [44] suggest a noticeable amount of radiative transitions (i.e., relatively large fluorescence yields) in certain quasisymmetric configurations of high-lying doubly excited Ar^{16+} states.

In this paper, we focus on resonant electron exchange and the emission of projectile Auger electrons during and after the collision. In Sec. II we give a brief overview of the dynamical classical overbarrier model for collisions of slow ions with spherical clusters. Details of this approach have been published elsewhere [21]. Being an essentially classical model, our approach requires a relatively small amount of information on the target-electronic structure, such that the target is sufficiently represented by its sequence of ionization potentials and its spectrum of bound states, including level degeneracies and occupations. More detailed information, e.g., given by electronic wave functions, is not required. For the target–electronic structure, we use results of the DFS calculation [23,27], a brief summary of which is given in

Sec. III. Once a hollow ion has been generated in an ion-cluster collision, it will start to decay on its way to the projectile detector. In Sec. IV we present a simple scheme that models this downstream decay as a sequence of autoionizing and radiative relaxation steps. Section V contains our numerical results and their discussion, and our conclusions follow in Sec. VI. Unless otherwise specified, we use atomic units throughout this work.

II. SUMMARY OF THE DYNAMICAL CLASSICAL OVERBARRIER MODEL

During the interaction with the projectile, energy levels, level occupations, transition rates, and total charges of target (q_t) and projectile (q_p) vary as a function of R , the internuclear distance between the target center of mass and the projectile. For the slow collisions considered in this work, an adiabatic approximation is justified, and it can be assumed that R does not change on the time scale of resonant electronic transitions.

We describe the projectile within an independent-electron approach based on hydrogenic shells n with energy levels, occupations numbers, and degeneracies denoted by $\epsilon_n^p(R)$, $a_n(R)$, and $A_n = 2n^2$. We do not resolve angular momentum sublevels. During the collision, the projectile energy levels shift due to image-charge effects, Stark shifts induced by a charged target, and the dynamical change in screening induced by varying level populations. Target energy levels $\epsilon_m^t(R)$ are Stark shifted downward in the electric field of the positive projectile. After the capture of target electrons, positive charge accumulates on the target, which results in an additional downward shift of the target spectrum.

In order to be captured (or recaptured), the active electron is required to overcome the potential barrier V_B between target and projectile that is formed by the total electronic potential

$$V(q, Q, R, z) = -\frac{q}{|R-z|} - \frac{Q}{z} + V_{\text{im}}(q, R, z), \quad (2.1)$$

where q and Q are the charges of projectile and target acting on the electron in transition. The electron coordinate along the internuclear axis is denoted by z . The image potential V_{im} includes the active electron’s self-image and the image potential of the effective projectile charge q . As the projectile approaches the target, the first resonant transfer of an electron becomes possible when V_B energetically moves below the highest occupied target level (or Fermi level), $\epsilon_F(R)$. The distance R_1^* , at which this may happen, is obtained numerically from the condition

$$\epsilon_F(R_1^*) = V_B(q, Q, R_1^*), \quad (2.2)$$

where $q = q_p(t = -\infty)$ and $Q = 1$. The generalization of this condition leads to decreasing critical radii $R_1^* > R_2^* > R_3^* \cdots$ for the sequential capture of electrons on the incoming trajectory.

The critical distances R_i^* for sequential overbarrier capture are related to geometrical cross sections for the production of specific charge states, $+i$, of C_{60} by

$$\sigma_i = \pi(R_i^{*2} - R_{i+1}^{*2}), \quad (2.3)$$

and to the total geometrical cross section $\sigma_{\text{tot}} = \pi R_1^{*2}$. The critical overbarrier distances can easily be extracted from the calculated impact-parameter-dependent final charge states of the target.

From the known initial occupations of target and projectile, a_n^0 and b_m^0 , the time evolution of the occupations $a_n(t)$ and $b_m(t)$ of projectile levels n and target levels m , and the emitted electron yield are obtained by integrating classical rate equations of the form

$$\frac{d}{dt} a_n = \Gamma_{\text{RN}} - \Gamma_{\text{RL}} a_n + \sum_{n' > n} \Gamma_{n', n} - 2 \sum_{n' < n} \Gamma_{n, n'}, \quad (2.4)$$

$$\frac{d}{dt} b_m = \Gamma_{\text{RL}} - \Gamma_{\text{RN}}. \quad (2.5)$$

Analytical expressions for the resonant-capture rates Γ_{RN} , resonant-loss rates Γ_{RL} , and Auger-transition rates are given in Ref. [21]. All rates and occupation numbers implicitly depend on $R(t)$, and the above equations are solved simultaneously with Newton's equation for the projectile motion.

Fast Auger transitions may partly relax a multiply excited projectile while competing resonant electron transfer occurs. With respect to Auger processes and during the collision, we therefore include fast transitions, for which the two active electrons start in the same shell. The basic Auger transition rates γ_{n_i, n_f} for the transition of an electron from initial shell n_i to final shell n_f accompanied by the emission of an electron out of shell n_i are given in Ref. [2]. In this reference the Cowan code [45] has been applied to the decay of highly excited $1sn_i s^2$ initial configurations to final configurations $1sn_f s \epsilon s$ with kinetic energies of the ejected electron $\epsilon < 4$ eV, and the numerical results were found to obey the scaling rule

$$\gamma_{n_i, n_f} = \frac{5.06 \times 10^{-3}}{(n_i - n_f)^{3.46}} = \frac{2.09 \times 10^{14} \text{ s}^{-1}}{(n_i - n_f)^{3.46}}. \quad (2.6)$$

We describe the dependence of Auger rates on the number of electrons in the initial and final active shells by statistical weights

$$\omega_{n_i}^i = \frac{1}{2}(a_{n_i}^2 - a_{n_i}), \quad (2.7)$$

and, as given in Ref. [2],

$$\omega_{n_f}^f = (1 + 1.5a_{n_f})^{-1}, \quad (2.8)$$

such that the Auger rates in Eq. (2.4) are given by

$$\Gamma_{n_i, n_f} = \omega_{n_i}^i \omega_{n_f}^f \gamma_{n_i, n_f}. \quad (2.9)$$

The statistical weight $\omega_{n_i}^i$ was previously found to parametrize (within limits) the dependence of Auger rates on the number of electrons in the initial active shell [46,41].

Vaeck and Hansen provided lower limits for total Auger decay rates Γ_{VH} of $1snp^{a_n}$ configurations in $\text{N}^{(6-a_n)+}$ ions (Fig. 1 in Ref. [41]), based on Cowan-code calculations [45]. Their ratios $\Gamma_{\text{VH}}(1s 10p^{a_n}) / \Gamma_{\text{VH}}(1s 10p^2)$ for initial occu-

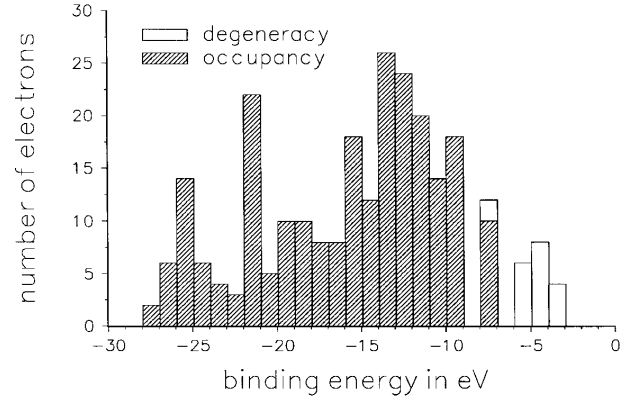


FIG. 1. Binding energies, degeneracies, and occupancies for the valence levels of C_{60} . All energy levels are binned in 1-eV intervals. Results of the Dirac-Fock-Slater calculation [23,27].

pations of the $n=10$ shell $a_{10}=2, 4,$ and 6 yield 1, 5, and 25, respectively, in fair agreement with the statistical weights (2.7). A detailed comparison of our Auger rates (2.9) with *ab initio* calculations is impossible, since such calculation have not yet been performed for the highly charged ions in multiply excited states of relevance in this paper. However, the lower limits for the Auger decay of $1snp^6$ configurations in Ar^{11+} ions given by Vaeck and Hansen (Fig. 5 in Ref. [41]) are of the same order of magnitude as our rates given by Eq. (2.9). For example, for the $n=10$ shell, Vaeck and Hansen find the lower limits $\Gamma_{\text{VH}}(1s 10p^6) = 5.6 \times 10^{13} \text{ s}^{-1}$, whereas Eq. (2.9) gives $\Gamma_{10, n_f} = 1.4 \times 10^{13}$ and $4.5 \times 10^{13} \text{ s}^{-1}$ for $n_f=8$ and 7 , respectively.

So far, slow Auger relaxation channels are not included as they can be neglected *during* the collision. Further downstream, however, when resonant transfer processes are classically forbidden, Auger processes determine the final charge state of the projectile. For the highly charged projectile studied in this paper, downstream Auger and radiative relaxation steps are accounted for by enhancing our dynamical simulation with a simple relaxation scheme (Sec. IV).

Projectile Auger electrons, emitted at time t with energy $\epsilon_A(t)$, are collected in energy bins $[\epsilon_k] \equiv [(k-1)\Delta\epsilon, k\Delta\epsilon]$, $k=1, 2, \dots$, with widths $\Delta\epsilon$ of the order of the experimental energy resolution. The numbers $c_k(t)$ of electrons emitted in each energy bin before time t and for a particular projectile trajectory are given by

$$\frac{d}{dt} c_k = \sum_{n_f} \sum_{n_i > n_f} \Gamma_{n_i, n_f} \times \begin{cases} 1 & \text{if } \epsilon_A(t) \in [\epsilon_k] \\ 0 & \text{otherwise.} \end{cases} \quad (2.10)$$

The overbarrier model is limited to impact parameters larger than a certain minimal value b_{min} . For relatively small charge states of the incident projectile, e.g., for N^{5+} , this value is given by the geometrical extension of the target [22]. For higher initial projectile charges, e.g., for Ar^{8+} [21] and certainly for Bi^{46+} , multiple-electron capture at impact parameters larger than the target radius may lead to fragmentation of the target. The overbarrier model can be applied to impact parameters that result in capture-induced fragmentation if the corresponding fragmentation time-scale is large

compared with the collision time. A conservative estimate for b_{\min} is given by the onset of the production of target charge states that lead to fragmentation during the collision. Recent experiments [25] suggest that for $q \leq 8$ the lifetime of C_{60}^{q+} is at least $5 \mu\text{s}$. However, for larger charge states q , fragmentation will be faster and might occur during the collision. In this case, the projectile might strongly interact with fragments, requiring the extension of the overbarrier model towards the inclusion of fast fragmentation channels.

Our version of the classical overbarrier model [21,22] approximates the target dielectric response to the external charges of active electrons and projectile ion by classical image potentials that are limited to the range of applicability of linear-response theory. The onset of nonlinear response imposes an upper limit for the projectile charge and a lower limit for the impact parameter. The distance R_{NL} of a charge q_p from a metal surface at which linear response theory starts to fail has been given by [3]

$$\tilde{R}_{\text{NL}} = 1.13 r_s \sqrt{q_p(\tilde{R}_{\text{NL}})}, \quad (2.11)$$

where r_s is the Wigner-Seitz radius of the target electron gas. For spherical conducting targets of sufficiently large radius, we may use this relation to obtain an estimate for the onset of nonlinear effects. The corresponding minimal distance from the target center of mass R_{NL} is then

$$R_{\text{NL}} = R_{\text{target}} + 1.13 r_s \sqrt{q_p(R_{\text{NL}})}. \quad (2.12)$$

This leads to the critical charge for the onset of nonlinear response

$$q_p(R_{\text{NL}}) = \left[\frac{R_{\text{NL}} - R_{\text{target}}}{1.13 r_s} \right]^2. \quad (2.13)$$

In our application to C_{60} (which for the purpose of this estimate is regarded as a spherical shell of radius a and thickness Δa) we find [33] $r_s = 1.2$ and $R_{\text{target}} = a + \Delta a/2 = 9.5$. By plotting the right hand side of Eq. (2.13) as a function of R together with the simulated charge state evolution $q_p(R)$, the critical impact parameter b_{\min}^{NL} for the onset of nonlinear response is given by the intersection of the two curves (cf. Sec. V).

III. ON THE ELECTRONIC STRUCTURE OF C_{60}

In terms of single-electron wave functions ϕ_i for all electrons in the cluster, the Dirac kinetic-energy operator \mathbf{t} , the potential energy of the interaction of the electrons with the nuclei V^n , the direct Coulomb-interaction potential between the electrons V^c , the electron-electron exchange potential in the local approximation,

$$V^{\text{ex}}(\mathbf{r}) = -3\alpha \left[\frac{3}{8\pi} \rho(\mathbf{r}) \right]^{1/3}, \quad (3.1)$$

with fixed parameter $\alpha = 0.7$, and the electronic density

$$\rho(\mathbf{r}) = \sum_i n_i \phi_i^\dagger(\mathbf{r}) \phi_i(\mathbf{r}), \quad (3.2)$$

TABLE I. Ionization potentials of $C_{60}^{(i-1)+}$.

i	DFS (Theory) (eV)	Experiment (eV)	Reference
1	7.17	7.58 ± 0.04	[48]
2	10.59	12.25 ± 0.5	[47]
3	13.98	17.0 ± 0.7	[47]
4	17.37		
5	20.73		
6	24.09		
7	27.43		

with occupation numbers n_i , the total energy of the many-electron molecular system can be written as [23,27]

$$E = \sum_i \langle \phi_i | \mathbf{t} | \phi_i \rangle + \int \rho V^n d^3r + \frac{1}{2} \int \rho V^c d^3r + \frac{3}{4} \int \rho V^{\text{ex}} d^3r + \sum_{p>q} \frac{Z_p Z_q}{|R_p - R_q|}. \quad (3.3)$$

Application of the usual variational procedure to this energy functional leads to the single-particle DFS equations for the wave functions ϕ_i and energy eigenvalues ε_i

$$[t + V^n + V^c + V^{\text{ex}}] | \phi_i \rangle = \varepsilon_i | \phi_i \rangle, \quad i = 1, \dots, N. \quad (3.4)$$

These equations can be solved within a molecular-orbital linear combination of atomic orbitals (MO-LCAO) scheme, i.e., by expanding the molecular-orbital wave functions in symmetry-adapted wave functions χ_j , which themselves are expanded in four-component Dirac spinors ξ_{nkm}^ν at lattice points \vec{r}_ν with coefficients $w_{\nu nkm}^j$,

$$\phi_i(\mathbf{r}) = \sum_j c_{ij} \chi_j = \sum_j c_{ij} \sum_{\nu nkm} w_{\nu nkm}^j \xi_{nkm}^\nu. \quad (3.5)$$

The symmetry orbitals are created using the icosahedral point group. For the $1s$, $2s$, $2p_{1/2}$, and $2p_{3/2}$ atomic states, the atomic basis functions ξ_{nkm}^ν used for the construction of the symmetry orbitals are numerically obtained by solving the atomic DFS equations. The calculations were done using the bond distances 2.772 and 2.561 between the C atoms, corresponding to the radius $a = 6.681$ of the Buckminsterfullerene.

The DFS single-particle energies of neutral C_{60} in the ground state are represented in Fig. 1 in bins of 1 eV width. The DFS has also been applied [23,27] to C_{60}^{+i} ions for $i \leq 6$. The i th ionization potential (Table I) is obtained as the difference of the total energies of the systems $C_{60}^{+(i-1)}$ and C_{60}^{+i} . For the scattering part of our calculation (cf. Sec. II), we used the DFS ionization potentials for $i \leq 6$ and approximated higher ionization potentials I_i , $i > 6$ by taking into account the work necessary to remove a seventh, eighth, etc., electron from the surface of a uniformly charged sphere of

radius a , $I_i = I_1 + (i-1)/a$ [21]. Table I also shows measured ionization potentials [47,48].

IV. RELAXATION SCHEME FOR HOLLOW IONS

For extremely inverted projectile populations, such as generated in the case of incident Bi^{46+} , a very large number of possible autoionizing transitions leads to an even larger number of possible relaxation cascades. In principle, once the hollow ion energy levels for various charge states and all transition rates are known, all possible cascades could be sampled in a Monte Carlo approach. Alternatively, in a less elaborate approach, the relaxation path could be selected under the assumption that the largest rate determines the next relaxation step [38]. In view of uncertainties and technical difficulties in accurately describing the relaxation of even doubly excited states [34,36–40,42–44], it is evident that for the more extreme cases of multiply excited projectiles, a rigorous theoretical treatment of autoionizing and radiative decay cascades is presently not accessible. We therefore employ a simple relaxation scheme that is based on intuition, basic features of emitted electron spectra, and wave-function overlap arguments. Our scheme is closely related to the ideas of Benoit-Cattin *et al.* [34], Posthumus and Morgenstern [39], and Ali *et al.* [38]. We do not resolve angular momentum states within a shell of principle quantum number n . Two electrons participating in an Auger transition are initially in shells $n_{i,1}$ and $n_{i,2}$, with $\delta n_i = n_{i,1} - n_{i,2}$. For nonequivalent electrons we may assume $n_{i,1} > n_{i,2}$. An autoionizing transition may occur into shell n_f , with $\delta n_f = n_{i,2} - n_f$. With these definitions our relaxation scheme can be summarized as follows.

(Aa) Since Auger transitions are driven by electron-electron correlation in the initial state, the relaxation cascade is assumed to start with the smallest possible δn_i . For a given δn_i , highest priority is given to Auger transitions that depopulate the highest possible shell. Next, for given values of n_i and δn_i , we minimize δn_f . This agrees with the general observation of very strongly enhanced emitted electron energy spectra close to the continuum threshold, as well as with relatively large wave-function overlap between initial and final states. The relaxation cascade may now start in the highest shell with $\delta n_i = 0$ and the smallest possible δn_f . This pattern is repeated until the ion is stable with respect to Auger decay of equivalent electrons.

(Ab) The relaxation now proceeds with autoionizing transitions of nonequivalent electrons. Highest priority is given to the smallest possible $\delta n_i > 0$ (say $\delta n_i = 1$). Second highest priority is given to the largest $n_{i,1}$. Next on the priority list are the smallest possible δn_f . If transitions for a particular set of values ($\delta n_i, n_i, \delta n_f$) are saturated, δn_f is successively increased until no more transitions for the specified values of δn_i and n_i are possible. Next, n_i is successively decreased, while, as before, δn_f is minimized until autoionizing transitions for the given value of δn_i are saturated. At this point δn_i is increased by one, and n_i and δn_f are selected and prioritized as before. This pattern is repeated until further increase of δn_i does not enable further autoionizing transitions. As occupations have changed, possibly leading to highly excited states with two equivalent electrons, after each transition in (Ab) we go back to the beginning of (Aa).

(Ra) Radiative transitions may continue to relax the excited ion. For hydrogenic states, radiative transition probabilities are largest for the lowest-lying final states and, among those, for the lowest emitted photon energies [49]. We designate the lowest shell with at least one vacancy by n_{\min} and the highest occupied shell by n_{\max} . We try to radiatively fill vacancies in shell n_{\min} , by increasing n_i from $n_{\min} + 1$ to n_{\max} .

(Rb) Once shell n_{\min} is full, we determine the new value for n_{\min} , and repeat (Ra) until all inner vacancies are filled.

Our version of the classical overbarrier model (Sec. II) allows for noninteger occupations of projectile shells. For very large charge states of the incoming projectile, the relaxation scheme just described leads to projectiles that are relaxed only with respect to transitions of integer elementary charges. This may result in an accumulation of fractions of an elementary charge in many higher shells. Consistent with our mainly classical approach to the generation of hollow atoms, and in order to fully depopulate high-lying shells, we therefore removed the restriction of charge quantization in the relaxation process in the following way: The scheme (Aa) to (Rb) is first applied while enforcing charge quantization. In our applications to incident Bi^{46+} ions, this ‘‘first round’’ left the projectiles in multiply excited states with noninteger occupations in many Rydberg shells. The same relaxation scheme is subsequently applied a second time *without* enforcing charge quantization. The removal of charge quantization means that we allow for transitions of fractions of elementary charges, corresponding to classical currents. In view of configuration interactions (CI), we may interpret noninteger occupations as shell occupations that are averaged over CI-coupled configurations. In the same sense, the charge and photon fractions emitted during the relaxation of these states have a statistical interpretation. After each transition populations have changed, and we go back to (Aa) to (first) allow for transitions that obey charge quantization. In this way, we eventually obtain ions with, at the most, noninteger shell occupations in the outermost shell. These ions are now stable with respect to autoionizing and radiative transitions, and their potential energy has been carried away by either electrons or photons.

With respect to Auger transitions, we maximize the current of emitted electrons, as explained by the following example. Suppose shell n_i has an average occupation of 0.7. Suppose further that autoionization occurs by filling shell n_f , which had an average population of 1.5. The emitted electron current is now maximized by depleting shell n_i , which results in the (averaged) emission of 0.35 negative charge units and an average population in shell n_f of 1.85. Similarly, for radiative transitions, we allow for the largest possible photon current, as the following example illustrates. Suppose the K shell has an average population of 1.8, and is to be filled by a $K\alpha$ transition. If the average L -shell population is 0.3, 0.2 negative charge units radiatively fill the K shell, leaving the L shell with an average population of 0.1. Simultaneously and in the average, 0.2 photons are emitted.

V. NUMERICAL RESULTS AND DISCUSSION

In Fig. 2 we show the evolution of projectile and target charge states, and of the total number of Auger electrons

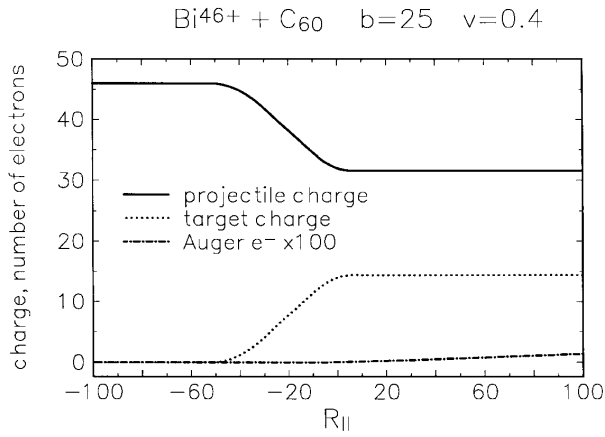


FIG. 2. Charge-state evolution for projectile and target and number of emitted Auger electrons for 830-keV (corresponding to a speed $v=0.40$ a.u.) Bi^{46+} ions colliding with C_{60} at impact parameter $b=25$ a.u. R_{\parallel} is the component along the direction of the incident projectile of the projectile position vector with respect to the target center of mass. The point of closest approach corresponds to $R_{\parallel}=0$.

emitted during the collision of 830-keV Bi^{46+} ions with neutral C_{60} for trajectories with impact parameter $b=25$. The distance R_{\parallel} is the projection of the target-projectile distance onto the incident-beam direction. The point of closest approach is given by $R_{\parallel}=0$. Charge exchange mainly occurs on the incident trajectory ($R_{\parallel}<0$), starting at $R_{\parallel}=-51.2$, which corresponds to the first critical overbarrier distance $R_{\parallel}^*=57.0$. For the considered impact parameter, about 14 electrons are resonantly captured. Resonant charge exchange ceases close to the distance of closest approach ($R_{\parallel}\approx 0$). For the displayed part of the trajectory, the charge-state evolution of the projectile is insensitive to projectile Auger transitions, as indicated by the very small current of emitted projectile electrons. This small current also indicates that the projectile is not relaxed at a distance of 100 downstream or, equivalently, 6 fs after its closest approach to the target. Our numerical studies show that, with respect to the fast Auger transitions included in Eq. (2.4), the projectile is relaxed at distances of about 10^4 a.u. downstream, or 600 fs after the closest approach. This time is an order of magnitude larger than the relaxation time found in grazing incidence collisions of 3.75 keV/amu $\text{O}^{3+\dots 9+}$ collisions with Au(110) surfaces [50]. The difference in time scales may be attributed to the comparatively long interaction time in the grazing ion-surface collisions, where relatively small impact parameters lead to the rapid direct filling of inner shells. This situation is very different from the large impact-parameter collisions considered in this work which resonantly populate high projectile shells (see subsequent discussion) and therefore require a multistep (and thus slow) transition cascade to relax the projectile.

A more detailed picture of the electronic transitions is given by the evolution of projectile [Fig. 3(a)] and target [Fig. 3(b)] level occupations. The impact parameter is the same as in Fig. 2. Figure 3(a) shows that resonant transitions first populate projectile shell $n=31$ and, as the projectile

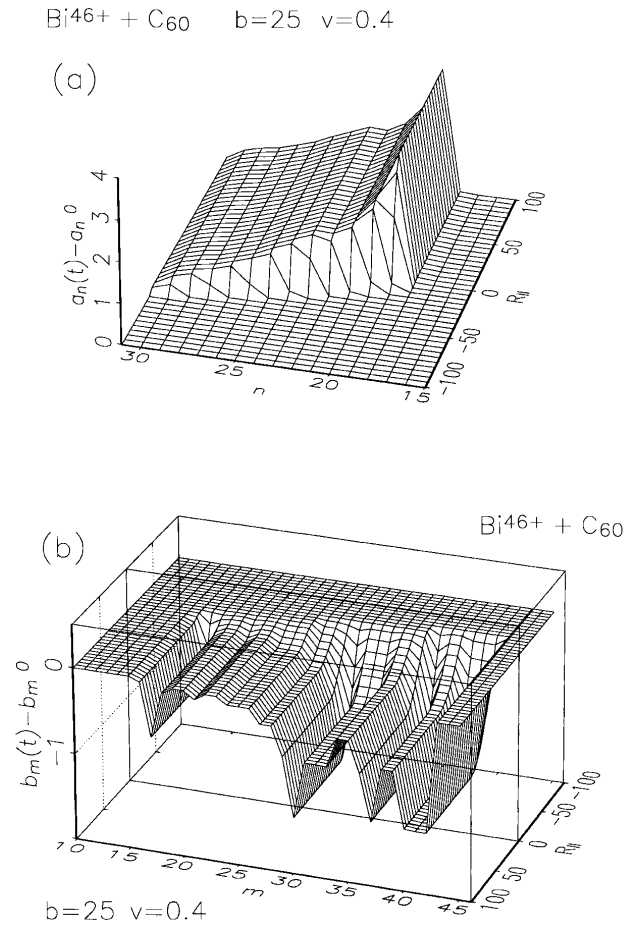


FIG. 3. Evolution of projectile and target level occupation changes with respect to the initial occupations. System and parameters as in Fig. 2. (a) Occupation changes of projectile levels n (main quantum number) as a function of R_{\parallel} . (b) Target occupation number changes. The quantum number m labels target levels as given by the Dirac-Fock-Slater calculation [23,27]. Quantum numbers $m\leq 17$ represent several levels binned in small energy intervals.

further approaches the target, eventually lead to the population of shells with principal quantum numbers between 19 and 31, thus providing a rather extreme case of population inversion.

Target energy levels are labeled with the quantum number m (not to be confused with a magnetic quantum number). As shown in Fig. 3(b), electrons are first captured out of the target Fermi level (labeled with the quantum number $m=42$), and next out of nearby levels below the Fermi level. Eventually, a large range of target levels becomes resonantly depopulated. In view of the large number of closely spaced valence levels of C_{60} and for computational convenience, we have introduced small (1 eV wide) energy bins that may contain several DFS target levels [23]. All quantum numbers $m\leq 17$ (corresponding to levels bound by more than 10.23 eV) in Fig. 3(b) represent bins that contain more than two electrons. For example, the energy bins $m=16$ and 17 are 24-fold and 20-fold degenerate, respectively. All numbers $m\geq 17$, with the exception of $m=30$, designate individual

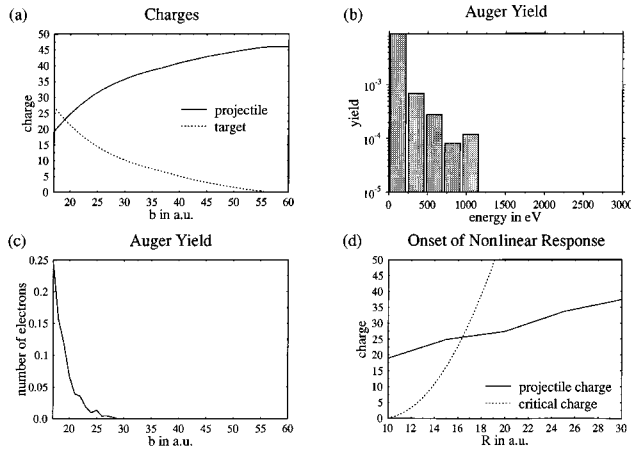


FIG. 4. (a)–(c) Results without downstream relaxation at $R_{\parallel} = 100$ a.u. downstream. (a) Projectile and target charge states. (b) Auger-electron yield, normalized, integrated over impact parameters, and binned in 234 eV energy intervals (see text). (c) Emitted projectile Auger electron yield per projectile as function of impact parameter. (d) Simulated projectile charge state on the incident trajectory for head-on collisions as a function of the distance to the target center-of-mass (solid line). Critical charge for the onset of nonlinear response (dotted line, cf (2.13)).

DFS levels. The quantum number $m=30$ marks an energy bin that includes two almost degenerate levels, and contains four electrons. The striking population changes at $m=16$ and 30 appear to be related to the relatively high degeneracy of the associated bins in the C_{60} valence spectrum and are, to some extent, an artifact of our particular energy binning.

Figures 2 and 3 allow for a simple estimate of the collision time, i.e., the time interval during which resonant transitions occur. The speed of $v=0.4$ and a typical path length for resonant interaction, $\Delta R_{\parallel} \approx 100$, yield a collision time of about $250=6$ fs. We have assumed that fragmentation of highly charged C_{60} ions does not change the charge exchange dynamics as simulated in the overbarrier model. This assumption becomes invalid should fragmentation happen on a time scale that is comparable or faster than the collision time.

Figure 4(a) shows charge states and emitted electron yields as a function of impact parameter and at a distance of $R_{\parallel} = 100$ downstream. At this distance resonant transfer is no longer possible. On the other hand, this distance is sufficiently small such that the projectile did not yet start to relax in any significant way, as is seen in the very small Auger yields in Figs. 4(b) and 4(c).

Figure 4(d) shows the simulated projectile charge-state evolution $q_p(R)$ for head-on collisions and distances of the ion to the target center of mass $R \leq 10$, together with the critical charge for the onset of nonlinear response [the right-hand side of Eq. (2.13)]. The curves intersect at $R \approx 16.5$, and we found it appropriate to choose $b_{\min} = b_{\min}^{\text{NL}} = 17$ in order to avoid nonlinear effects. Our simulation is therefore restricted to collisions with $b \geq 17$, and all simulated spectra and yields shown below only include such distant collisions.

The spectrum of Auger electrons in Fig. 4(b) is given by the numbers c_k [Eq. (2.10)] of projectile electrons emitted in 234 eV wide energy bins by the time the projectile has

TABLE II. Critical overbarrier radii R_i^* (in a.u.), geometrical cross sections (in a.u.) for the production of final target charge states $+i$ in 830 keV Bi^{46+} on C_{60} collisions σ_i (in a.u.), and target charge fractions f_i , for impact parameters $b > 21$ a.u. The total cross section for charge-state changing collisions is $\sigma_{\text{tot}} = 1.02 \times 10^4$ a.u. $= 2.86 \times 10^{-13}$ cm².

i	R_i^*	$\sigma_i/100$	f_i
1	57.0	17.1	0.17
2	52.0	10.4	0.10
3	48.7	10.0	0.098
4	45.3	7.19	0.071
5	42.7	6.51	0.064
6	40.2	4.93	0.048
7	38.2	5.13	0.050
8	36.0	4.82	0.047
9	33.8	3.92	0.038
10	31.9	3.13	0.031
11	30.3	2.42	0.024
12	29.0	2.49	0.024

reached the distance $R_{\parallel} = 100$ (downstream) according to the expression for the yield y ,

$$y = \frac{2\pi}{A} \int_{b_{\min}}^{R_1^*} db b c_k(b). \quad (5.1)$$

We have normalized this energy differential yield to the area run through by projectiles on charge-state changing trajectories

$$A = \pi(R_1^{*2} - b_{\min}^2) = 8492.0. \quad (5.2)$$

We note that there is some uncertainty in the choice of b_{\min} . However, for very highly charged incident ions the first critical overbarrier radius is large compared with b_{\min} and πb_{\min}^2 small compared to A . Figure 4(c) shows the number of emitted projectile Auger electrons per projectile as a function of impact parameter when the projectile reaches the distance $R_{\parallel} = 100$ (downstream).

From the target charge versus impact parameter dependence [Fig. 4(a)] the sequence of critical radii R_i^* for the capture of one, two, etc., electrons can be extracted. The exact values of our simulation are listed in Table II, together with the corresponding geometrical cross sections σ_i [Eq. (2.3)], for the production of a specific target charge state i , and the fraction $f_i = \sigma_i/\sigma_{\text{tot}}$ of produced fullerene ions with charge $+i$. The total cross section for charge-state changing collisions is $\sigma_{\text{tot}} = 1.02 \times 10^4 = 2.86 \times 10^{-13}$ cm² and is significantly larger than the calculated total cross sections for Ar^{8+} (6.2×10^{-14} cm²) [21] and N^{5+} (4.3×10^{-14} cm²) [22] projectiles. Figure 5 shows the fractions f_i for $i \leq 20$, corresponding to distant collisions with $b > 21$. These fractions represent 87% of all recoil ion charge states ($\sum_1^{20} f_i = 0.87$). The remaining 13% represent recoil ions that are generated at impact parameters smaller than 21. Interestingly, our simulated fullerene ion charge-state distribution does not have the binomial shape proposed by Jin *et al.* [25]. At this point the reason for this discrepancy is not known,

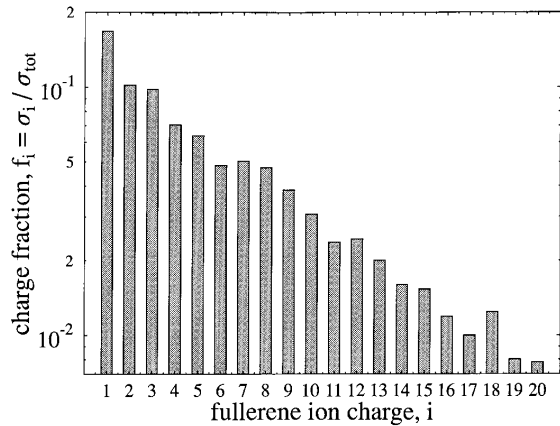


FIG. 5. Distribution of target charge states immediately after resonant charge exchange has ceased at $R_{\parallel}=100$ a.u. downstream for impact parameters $b>21$ a.u.

and might be assigned to deficiencies in our simulation. We note, however, that Jin *et al.* applied a binomial fit to their measured charge state distribution which is based on the assumptions that (1) multiple electron capture proceeds as a sequence of independent capture events with *identical* capture probabilities, and (2) only a small fraction of all delocalized electrons in C_{60} are available for capture.

In Fig. 6 we present our results including downstream projectile relaxation as described in Sec. IV. As a consequence of the downstream relaxation process, most of the captured electrons are autoionized, as is easily seen by comparing Fig. 6(a) with 4(a). Due to this long-range relaxation process, the incident projectile charge effectively changes at the most by a few units, for the closest considered collisions. In comparison with Figs. 4(b) and 4(c), Figs. 6(b) and 6(c) show that autoionization is practically restricted to downstream deexcitations that happen after the collision, as a simple order-of-magnitude comparison of the collision time and typical Auger transition times suggests. The same is true for the in general slower radiative transitions. Radiative transitions only contribute to the relaxation, while the projectile moves a macroscopic distance between the collision region and detector. We note that our emitted electron yields and, more so, our radiative yields are tentative, due to the complicated nature of both, the primary capture events and the relaxation process. For the considered range of impact parameters ($b \geq 17$), we find a total branching ratio (total x-ray yield divided by total Auger yield) of 0.03.

VI. SUMMARY AND CONCLUSIONS

Within the dynamical classical overbarrier model for collisions of slow ions with spherical clusters, we simulated the formation of hollow ions during the interaction of very highly charged bismuth ions with C_{60} . In the description of the target electronic structure, we relied on a recently performed DFS calculation for C_{60} and its positive ions. We calculated cross sections for the production of specific target-charge states as well as charge-state and occupation evolutions of both collision partners during the collision, i.e.,

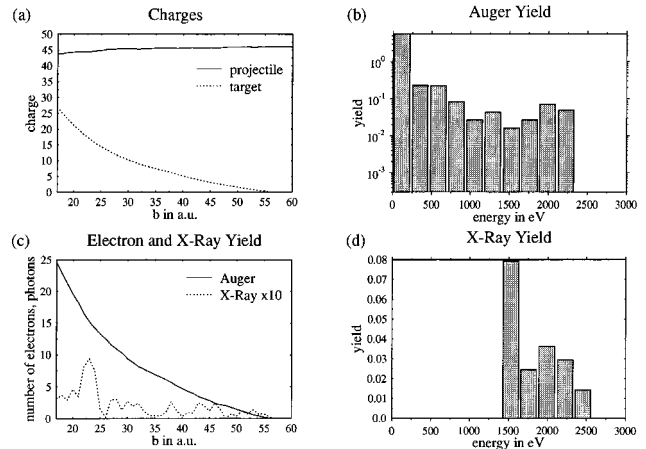


FIG. 6. Results including downstream relaxation. (a) Projectile and target charge states. (b) Auger-electron yield, normalized, integrated over impact parameters, and binned in 234-eV energy intervals (see text). (c) Emitted projectile Auger-electron yield and photon yields per projectile as functions of impact parameter. (d) X-ray yield, normalized, integrated over impact parameters, and binned in 234-eV energy intervals.

while resonant exchange channels are open. In contrast to previous investigations [25] that predict a binomial distribution of collisionally produced target charge states, we find a charge-state distribution which, in trend, decreases with increasing charge of the target.

We further investigated the downstream relaxation of collisionally produced hollow ions, and proposed a simple relaxation scheme that includes both autoionizing and radiative transitions. This scheme allows for the simulation of energy differential and total yields of Auger electrons and photons, emitted while the projectile relaxes. As a result of this downstream relaxation, we find that almost all of the resonantly captured electrons are emitted due to autoionization, while the projectile moves away from the interaction region.

Future investigations, both experimental and theoretical, are necessary to improve our understanding of many-electron transfer processes and emitted electron and x-ray spectra in collisions between highly charge ions and clusters. Due to the complexity of the collision system, nonperturbative *ab initio* calculations, based on quantum-mechanical matrix elements, are currently out of reach. On the other hand, the many-electron nature of the hollow ion formation and decay leads us to believe that not all the detailed information provided by first-principles calculations is needed to describe the processes considered in this paper. Much of the quantum-mechanical details will be averaged over and out. In this sense, simple models, successively refined and fine tuned to future experiments, will contribute to a better understanding of the complex nature of the formation and decay of hollow ions.

ACKNOWLEDGMENTS

The author is grateful to C. L. Cocke for stimulating discussions. This work was supported by the Division of Chemical Sciences, Basis Energy Sciences, Office of Energy Research, U.S. Department of Energy.

- [1] M. Schulz, C. L. Cocke, S. Hagmann, and M. Stöckli, *Phys. Rev. A* **44**, 1653 (1991).
- [2] J. Burgdörfer, P. Lerner, and F. W. Meyer, *Phys. Rev. A* **44**, 5674 (1991).
- [3] J. Burgdörfer, in *Review of Fundamental Processes and Applications of Atoms and Ions*, edited by C. D. Lin (World Scientific, Singapore, 1993), p. 517.
- [4] J. Burgdörfer, C. Reinhold, and F. W. Meyer, *Nucl. Instrum. Methods Phys. Res. Sect. B* **98**, 415 (1995).
- [5] B. d'Etat, J. P. Briand, G. Ban, L. de Billy, J. P. Desclaux, and P. Briand, *Phys. Rev. A* **48**, 1098 (1993).
- [6] F. W. Meyer, C. C. Havener, and P. A. Zeijlmans van Emmichoven, *Phys. Rev. A* **48**, 4476 (1993).
- [7] H. Kurz, F. Aumayr, H. P. Winter, D. Schneider, M. A. Briere, and J. W. McDonald, *Phys. Rev. A* **49**, 4693 (1994).
- [8] M. Grether, A. Spieler, R. Köhrbrück, and N. Stolterfoht, *Phys. Rev. A* **52**, 426 (1995).
- [9] R. Page, A. Saal, J. Thomaschewski, L. Aberle, J. Bleck-Neuhaus, R. Köhrbrück, M. Grether, and N. Stolterfoht, *Phys. Rev. A* **52**, 426 (1995).
- [10] C. J. Setterlind and A. Bárány, *Nucl. Instrum. Methods Phys. Res. Sect. B* **98**, 407 (1995).
- [11] J. Limburg, S. Schippers, I. Hughes, R. Hoekstra, R. Morgenstern, S. Hustedt, N. Hatke, and W. Heiland, *Phys. Rev. A* **51**, 3873 (1995).
- [12] J. P. Briand, B. D'Etat-Ban, D. Schneider, M.A. Briere, V. Decaux, J.W. McDonald, and S. Bardin, *Phys. Rev. A* **53**, 2194 (1996).
- [13] S. Winecki, C. L. Cocke, D. Fry, and M. P. Stöckli, *Phys. Rev. A* **53**, 4228 (1996).
- [14] A. G. Borisov, R. Zimny, D. Teillet-Billy, and J. P. Gauyacq, *Phys. Rev. A* **53**, 2457 (1996).
- [15] J. Limburg, S. Schippers, R. Hoekstra, R. Morgenstern, H. Kurz, F. Aumayr, and H. P. Winter, *Phys. Rev. Lett.* **75**, 217 (1995).
- [16] T. Neidhart, F. Pichler, F. Aumayr, H. P. Winter, M. Schmid, and P. Varga, *Phys. Rev. Lett.* **75**, 217 (1995).
- [17] F. Aumayr, in *Proceedings of the XIX International Conference on the Physics of Electronic and Atomic Collisions*, edited by L. J. Dubé, J. B. A. Mitchell, J. W. McConkey, and C. E. Brion, AIP Conf. Proc. No. 360 (AIP, New York, 1995), p. 631.
- [18] C. Auth and H. Winter (unpublished).
- [19] B. Walch, C. L. Cocke, R. Voelpel, and E. Salzborn, *Phys. Rev. Lett.* **72**, 1439 (1994).
- [20] T. LeBrun, H. G. Berry, S. Cheng, R. W. Dunford, H. Esbensen, D. S. Gemmel, and E. P. Kanter, *Phys. Rev. Lett.* **72**, 3965 (1994).
- [21] U. Thumm, *J. Phys. B* **27**, 3515 (1994).
- [22] U. Thumm, *J. Phys. B* **28**, 91 (1995).
- [23] U. Thumm, T. Baştug, and B. Fricke, *Phys. Rev. A* **52**, 2955 (1995).
- [24] A. Bárány and C. J. Setterlind, *Nucl. Instrum. Methods Phys. Res. Sect. B* **98**, 184 (1995).
- [25] J. Jin, H. Khemliche, M.H. Prior, and Z. Xie, *Phys. Rev. A* **53**, 615 (1996).
- [26] H. Winter, *Europhys. Lett.* **18**, 207 (1992).
- [27] T. Baştug, P. Kürpick, J. Meyer, W.-D. Sepp, and B. Fricke (unpublished).
- [28] S. Satpathy, *Chem. Phys. Lett.* **130**, 545 (1986).
- [29] S. Saito and A. Oshiyama, *Phys. Rev. Lett.* **66**, 2637 (1991).
- [30] J. H. Weaver, J. L. Martins, T. Komeda, Y. Chen, T. R. Ohno, G. H. Kroll, N. Troullier, R. E. Haufler, and R. E. Smalley, *Phys. Rev. Lett.* **66**, 1741 (1991).
- [31] J. L. Martins, N. Troullier, and J. H. Weaver, *Chem. Phys. Lett.* **180**, 457 (1991).
- [32] C. Yannouleas and U. Landman, *Chem. Phys. Lett.* **217**, 175 (1994).
- [33] M. J. Puska and R. M. Nieminen, *Phys. Rev. A* **47**, 1181 (1993).
- [34] P. Benoit-Cattin, A. Bordenave-Montesquieu, M. Boudjema, A. Gleizes, S. Dousson, and D. Hitz, *J. Phys. B* **21**, 3387 (1988).
- [35] A. Niehaus, *J. Phys. B* **19**, 2925, (1986).
- [36] R. Ali, C. L. Cocke, M. L. A. Raphaelian, and M. Stöckli, *J. Phys. B* **26**, L117 (1993).
- [37] P. Roncin, M. N. Gaboriaud, and M. Barat, *Europhys. Lett.* **16**, 551 (1991).
- [38] R. Ali, C. L. Cocke, M. L. A. Raphaelian, and M. Stöckli, *Phys. Rev. A* **49**, 3586 (1994).
- [39] J. H. Posthumus and R. Morgenstern, *Phys. Rev. Lett.* **68**, 1315 (1992).
- [40] N. Vaeck and J. E. Hansen, *J. Phys. B* **24**, L469 (1991); **25**, 3267 (1992).
- [41] N. Vaeck and J. E. Hansen, *J. Phys. B* **28**, 3523 (1995).
- [42] H. W. van der Hart and J.E.Hansen, *J. Phys. B* **26**, 641 (1993).
- [43] J. E. Hansen, O. Schraa, and N. Vaeck, *Phys. Scr.* **T41**, 41 (1992).
- [44] Z. Chen and C. D. Lin, *J. Phys. B* **26**, 957 (1993).
- [45] R. D. Cowan, *The Theory of Atomic Structure and Spectra* (University of California Press, Berkeley 1981).
- [46] E. J. McGuire, *Phys. Rev.* **185**, 1 (1969).
- [47] C. Lifshitz, M. Iraqi, T. Peres, and J. E. Fischer, *Rapid Commun. Mass Spectrom.* **5**, 238 (1991).
- [48] I. V. Hertel, H. Steger, J. de Vries, B. Weisser, C. Menzel, B. Kamke, and W. Kamke, *Phys. Rev. Lett.* **68**, 784 (1992).
- [49] E. U. Condon and G. H. Shortley, *The Theory of Atomic Spectra* (Cambridge University Press, Cambridge, 1957), pp. 136 and 148.
- [50] L. Folkerts, S. Schippers, D. M. Zehner, and F. W. Meyer, *Phys. Rev. Lett.* **74**, 2204 (1995).